

Inverse design of a Helmholtz resonator based low-frequency acoustic absorber using deep neural network

Cite as: J. Appl. Phys. **129**, 174901 (2021); doi: [10.1063/5.0046582](https://doi.org/10.1063/5.0046582)

Submitted: 4 February 2021 · Accepted: 14 April 2021 ·

Published Online: 3 May 2021



K. Mahesh,¹ , S. Kumar Ranjith,^{1,2} and R. S. Mini^{1,a)}

AFFILIATIONS

¹Department of Mechanical Engineering, College of Engineering Trivandrum (Government of Kerala), Thiruvananthapuram 695016, Kerala, India

²Micro/Nanofluidics Research Laboratory, Department of Mechanical Engineering, College of Engineering Trivandrum (Government of Kerala), Thiruvananthapuram 695016, Kerala, India

^{a)}Author to whom correspondence should be addressed: rsmini@cet.ac.in

ABSTRACT

The design of low-frequency sound absorbers with broadband absorption characteristics and optimized dimensions is a pressing research problem in engineering acoustics. In this work, a deep neural network based inverse prediction mechanism is proposed to geometrically design a Helmholtz resonator (HR) based acoustic absorber for low-frequency absorption. Analytically obtained frequency response from electro-acoustic theory is deployed to create the large dataset required for training and testing the deep neural network. The trained convolutional neural network inversely speculates optimum design parameters corresponding to the desired absorption characteristics with high fidelity. To validate, the inverse design procedure is initially implemented on a standard HR based sound absorber model with high accuracy. Thereafter, the inverse design strategy is extended to forecast the optimum geometric parameters of an absorber with complex features, which is realized using HRs and a micro-perforated panel. Subsequently, a quasi-perfect low-frequency acoustic absorber having minimum thickness and broadband characteristics is deduced. Importantly, it is demonstrated that the proposed absorber, comprising four parallel HRs and a microperforated panel, absorbed more than 90% sound in the frequency band of 347–630 Hz. The introduced design process reveals a wide variety of applications in engineering acoustics as it is suitable for tailoring any sound absorber model with desirable features.

Published under an exclusive license by AIP Publishing. <https://doi.org/10.1063/5.0046582>

I. INTRODUCTION

Noise is considered as one of the pervasive environmental pollutants that adversely affects human health and wildlife. In particular, low-frequency sound emission from aircraft, road traffic, wind turbines, and air conditioning units can propagate a long distance with less attenuation and can cause annoyance, sleep disturbance, fatigue, cardiovascular problems, and hearing impairment.^{1–5} Thereby, effective mitigation of low-frequency noise is a challenging problem in engineering acoustics. Indeed, natural structures such as trees and vegetation or artificial structures such as walls or highway barriers are not sufficient to stop the propagation of low-frequency noise.^{6,7} Even traditional passive absorbers such as fibrous or porous materials are needed to be extremely bulky to attenuate this low-frequency noise.⁸ Resonant absorbers such as

Helmholtz resonators (HRs)^{9–11} and microperforated panels (MPPs)^{12–14} are widely used as alternatives to traditional sound absorbers for low-frequency applications. However, a tradeoff for this low-frequency sound abatement is the requirement of long cavities; hence, alterations to the conventional resonant absorbers are essential. In this regard, Sakagami *et al.*¹⁵ combined MPPs of different absorption characteristics to extend the absorption spectrum to the low-frequency regime. Later, Li *et al.*¹⁶ suggested a parallel arrangement of perforated panels to absorb low-frequency sound. Moreover, the modifications of cavity shape¹⁷ and arranging MPPs of different cavity depths¹⁸ are found to be effective. Meanwhile, tailoring the geometry of conventional Helmholtz resonators proved to be effective for low-frequency sound absorption with minimized thickness.^{19–23} Recently, Guo *et al.*²⁴ achieved quasi-perfect sound absorption in an absorber comprising a parallel array

of Helmholtz resonators with an extended neck. They further extended the study to minimize the absorber thickness using HRs of an embedded spiral neck.²⁵ Similarly, the usage of roughened embedded neck exhibited significant improvement in the low-frequency sound absorption.²⁶ However, these strategies yield relatively narrow absorption bandwidth, which inevitably hinders practical applications. Thus, the development of a low-frequency sound absorber with minimum thickness and broadband absorption characteristics is an active research question that requires better solutions.

The aforementioned issue is partially addressed in the previous work,²⁷ which proposed a low-frequency sound absorber of thickness 5.6 cm with an effective absorption bandwidth of more than four one-third octave bands. That model was an integration of different Helmholtz resonators with inserted neck (HRINs) and MPP. However, the dimensions of the particular model are not optimized for targeted absorption characteristics. To this end, the selection of suitable dimensions from desired absorption characteristics, known as an inverse design, is necessary. It is noteworthy that the conventional optimization techniques or inverse mathematical models are not sufficient to deal with the computational complexity of practical inverse design problems.^{28–30} Furthermore, the traditional prediction or optimization procedure is extremely time consuming and error prone.³¹ Conventional inverse design techniques mainly rely on genetic algorithm,³² topology optimization,³³ particle swarm methods,³⁴ level-set methods,³⁵ and so on. However, these methods are constrained by the random search process, which typically leads to local optima rather than reaching a preferred global optimum.^{36–38} Moreover, such schemes are computationally expensive owing to their inherent iterative nature and requirement of full field numerical simulation.^{36,37,39} Apart from these shortcomings, inverse design problems are affected by ill-posedness, where the problem does not have a unique feasible solution or it may have multiple infeasible solutions.^{40,41} However, ill-posedness can be reduced to some extent by regularization methods such as the Tikhonov method,⁴² the single value decomposition method,⁴³ the L2 regularization method,⁴⁴ etc. Nevertheless, these methods are highly sensitive so that a minor variation in inputs results in a large deviation in outputs. On the other hand, due to the faster convergence rate, gradient based optimization methods such as the adjoint method are considered as an alternative for conventional stochastic search algorithms. However, it will also succumb to local minima and the solutions can be quite non-trivial.^{28,45} Moreover, Sun *et al.*⁴⁶ showed that evolutionary/gradient approaches like genetic algorithm (GA) often require hundreds of generations to reach an optimum solution. Meanwhile, data-driven approaches demonstrate a significant improvement in prediction accuracy, time consumption and computational efficiency. In this context, data-driven approaches based on machine learning (ML) are assumed important to solve these kinds of inverse problems with high accuracy.^{29,31,47}

Machine learning is an application of artificial intelligence (AI) that allows computer algorithms to learn and improve with experience.⁴⁸ AI has enjoyed a resurgence in recent years with the help of enhanced computational power and data availability. Acoustics also reap the rewards by minimizing the effort and improving the results and a few problems in the domain are solved

with the help of artificial neural networks (ANNs).^{49–52} Jeon *et al.*⁵⁰ proposed an ANN model to predict the sound absorption coefficient of layered fibrous material while Iannace *et al.*⁵¹ used ANN to predict the sound absorption coefficient of broom fibers. Similarly, Huang *et al.*⁵² used a deep neural network to predict the sound quality of vehicular noises. All these models are forward prediction techniques and their computational complexity is marginal. In contrast, machine learning based inverse design methods are rarely used in acoustics, though they are used frequently in other physical problems such as nano photonics,^{28,29,31,53,54} electromagnetic,⁵⁵ aerospace,⁵⁶ and acoustic cloaking.⁴⁷ As an exception, Zheng *et al.*⁵⁷ proposed a Gauss–Bayesian model for the inverse design of the acoustic metamaterial. This model starts with a random design and iteratively updates its parameters to reach an optimal design. Since it uses numerical computation in each iteration, its computational time is high and it is highly error prone. Data-driven approaches like deep neural networks (DNN) mitigate such shortcomings and produce results much faster with better accuracy and fidelity. To the best of the authors' knowledge, DNN based inverse prediction techniques are not yet used in designing sound absorbers.

In this study, a novel DNN based inverse method is developed to predict the geometric parameters of a low-frequency sound absorber from its acoustic functionalities. Since the considered configuration is a composite structure having microperforated panel embedded with Helmholtz resonators, it is an intrinsically complex problem with non-unique solutions. Hence, developing an inverse mathematical model to relate the absorption characteristics to the geometrical parameters is laborious. The dataset for training and testing of DNN is prepared using an analytical model based on electro-acoustic theory. Initially, with the help of custom made DNN, the inverse prediction method is successfully implemented on an established low-frequency HR based sound absorber model. Then, the inverse prediction technique is extended to design a low-mid frequency sound absorber (MPP with HR) of desired characteristics. This paper is structured as follows: the inverse prediction methodology, the briefing of the proposed DNN architecture, and its training and testing are detailed in Sec. II. Thereafter, in Sec. III, the inverse design of low-frequency sound absorber is detailed. Finally, the concluding remarks are dealt with in Sec. IV.

II. INVERSE DESIGN USING DEEP NEURAL NETWORK

First, the proposed inverse design methodology using the deep neural network is detailed for an acoustic absorber. The work flow chart of the inverse design using deep neural network (IDDN) is shown in Fig. 1. It is noteworthy that the present strategy is initially validated on a simple HR based absorber; thereafter, a complicated acoustic absorber realized using MPP embedded with HR is designed. Here, the generation of a dataset based on the input parameters is made initially in the forward direction, which is followed by inverse prediction of geometric parameters of absorber using DNN for a pre-determined response as depicted in Fig. 1(a). The systematic procedure of IDDN is enumerated as follows:

- (i) Select a suitable sound absorber for desired absorption characteristics. Note that for low/medium frequencies, an HR or

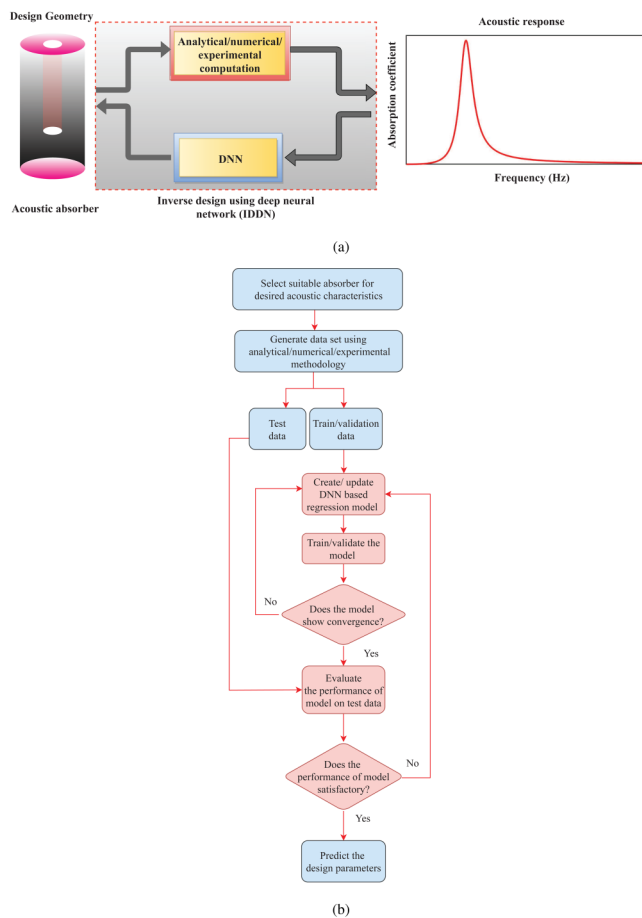


FIG. 1. Schematic illustration of the inverse design using the deep neural network (IDNN). (a) Dataset generation in the forward direction and inverse prediction in the backward direction. (b) Detailed flow chart of the IDNN procedure from input to output.

its combination with MPP can be employed. However, for high frequency applications, porous/fibrous absorbers can be selected. Further, the limiting values of the geometrical parameters of the absorber need to be chosen initially.

- (ii) Generate absorption characteristics corresponding to the desired frequency regime using analytical/numerical/experimental methodology. For generating a sufficient amount of data, the different combinations of geometrical (thickness, diameter, etc.) or acoustical (flow resistivity, porosity, etc.) parameters are selected.
- (iii) Segmentation of the generated dataset into three categories as train, validation, and test [see Fig. 1(b)]. The details of these exclusive sets are as follows:

Train set: The train dataset is used for training the DNN model. The DNN model sees and learns from these data. For proper training, the majority of available data (>80%) should be assigned as a train dataset.

Validation set: This set is used for the frequent evaluation of the trained model. The DNN model can see these data; however, it never learns from them.

Test set: This is a mutually exclusive dataset used for the unbiased evaluation of the trained DNN model. The model never sees or learns this data fragment.

- (iv) Create DNN to compute the inverse mapping between the input (absorption characteristics) and output (design parameters). Select suitable layers and layer parameters for the DNN model.
- (v) Train and validate the model using the train and validation dataset, respectively. Select suitable hyperparameters, objective function, and optimizer for the training process.
- (vi) If the model demonstrates convergence by satisfactory error rate, evaluate its performance on the test data, otherwise update the DNN model or tune the model by changing layer parameters or hyperparameters.
- (vii) If the performance of the model is satisfactory on the test data, then predict the design parameters using the final saved weights of the DNN model. Otherwise, update the DNN model or tune the model by changing layer parameters or hyperparameters.
- (viii) On successful completion of all these steps, optimized absorber geometries corresponding to the given input data are obtained. Further, the acoustic response from this absorber is compared with experimental or theoretical results to check the effectiveness of the scheme.

A. Selection of absorber and dataset generation

An existing sound absorber model [Helmholtz resonator with inserted neck (HRIN)] is chosen to validate the new methodology. The geometrical features of the optimal design are predicted from sound absorption characteristics using a trained neural network. The absorption characteristics obtained for the Helmholtz resonator with an embedded aperture proposed by Huang *et al.*²³ are used for this purpose. The physical model of HRIN is given in Fig. 2(a). The schematic diagram of HRIN with neck length l_N , neck radius r_N , cavity radius r_C , and cavity beyond neck length l_C is shown in Fig. 2(b). This absorber is selected because geometric parameters for this scenario are only four and experimental results are also accessible for subsequent comparison. Moreover, analytical solutions are available for this model²³ to obtain the acoustic responses for a wide range of input parameters. The dataset preparation, the custom DNN model, and the training and testing of the DNN for the inverse design of HRIN are detailed below.

The size of the dataset is a vital cog in a deep neural network training process, which significantly influences the accuracy of results. In this case, it is practically impossible to generate sufficient data required for training by experimental means. Hence, an analytical methodology is adopted to create a large amount of data for the training process. From the equivalent electro-acoustic representation of an HRIN shown in Fig. 2(c), the expression for the impedance⁵⁸ is written as

$$Z_{HR} = Z_{RN} + Z_{RC}, \quad (1)$$

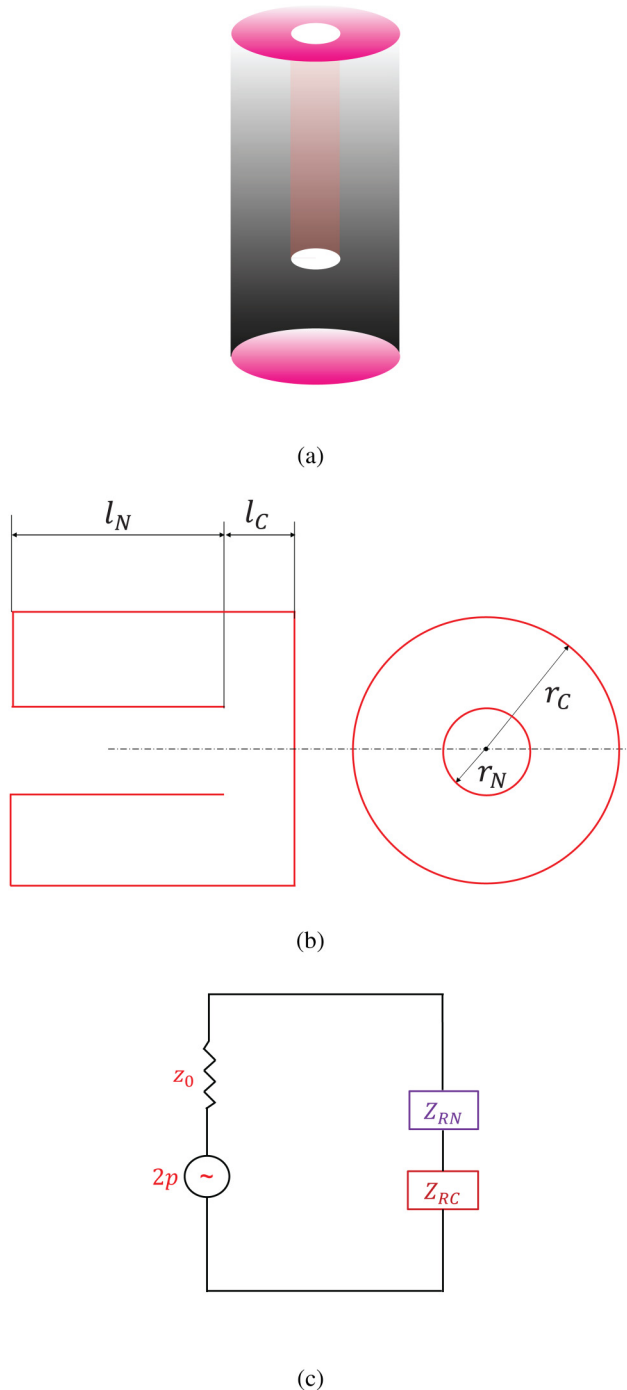


FIG. 2. (a) Physical model of Helmholtz resonator with inserted neck (HRIN), (b) its schematic diagram, where l_N is the neck length, l_C is the cavity beyond neck length, r_N is the neck radius, and r_C is the cavity radius, and (c) its equivalent electro-acoustic circuit, where Z_{RN} is the acoustic impedance of the resonator neck, Z_{RC} is the acoustic impedance of the resonator cavity, and z_0 is the specific acoustic impedance of air.

where Z_{RN} is the acoustic impedance of the resonator neck and Z_{RC} is the acoustic impedance of the resonator cavity. Moreover, Z_{HR} can also be written in terms of normalized specific acoustic resistance R_{HR} and normalized specific reactance X_{HR} as follows:⁵⁸

$$Z_{HR} = z_0(R_{HR} + jX_{HR}). \quad (2)$$

Note that the normalized specific acoustic resistance⁵⁸

$$R_{HR} = \frac{\sqrt{8\eta\rho\omega}((l_N/2r_N) + 1)}{\varepsilon_T\rho c}, \quad (3)$$

and the normalized specific acoustic reactance

$$X_{HR} = \frac{1}{\varepsilon_T}k(l_N + \delta) - \frac{1}{kl_{RC}}, \quad (4)$$

where η is the dynamic viscosity of air, ω is the angular frequency, ε_T is the perforation ratio, ρ is the density of air, c is the velocity of air, and k is the acoustic wave number. Here, $\varepsilon_T = S_n/A_0$, where S_n is the cross-sectional area of neck and A_0 is the cross-sectional area of the cavity. Modified cavity height $l_{RC} = l_N + l_C - \varepsilon_T l_e$, considers the effective length of the neck $l_e = l_N + \delta$, where $\delta = 1.7r_N$ is the end correction. Finally, the absorption coefficient, α , is determined using the relation

$$\alpha = 1 - \left| \frac{Z_{HR} - z_0}{Z_{HR} + z_0} \right|^2, \quad (5)$$

whose value is typically between 0 and 1.

Employing a custom python script, the absorption coefficients corresponding to an arbitrary set of four geometrical parameters are generated over a frequency range of 0–700 Hz using Eq. (5). Since the present study focuses on the design of low-mid frequency sound absorber, the frequency range is fixed as 0–700 Hz. During the dataset preparation, apart from the four geometric parameters, all other physical and material parameters are kept constant. At the same time, the values of each geometric variable are randomly generated within the suitable limits from a uniform distribution. These random values are rounded up to four significant digits. The dimensions chosen for the data preparation are given in Table I. A sample dataset of frequency response is depicted in Fig. 3, where all the parameters are fixed except r_N . Note that the peak absorption coefficient is different for different r_N values. In addition, the frequency corresponding to the peak absorption coefficient also changes, and the offset in values is evident in Fig. 3. To underline

TABLE I. Dimensions chosen for the dataset preparation for the prediction of geometrical parameters of HRIN.

Parameters	Limit of random values (mm)
l_N	10–100
r_N	1–10
l_C	5–50
r_C	10–50

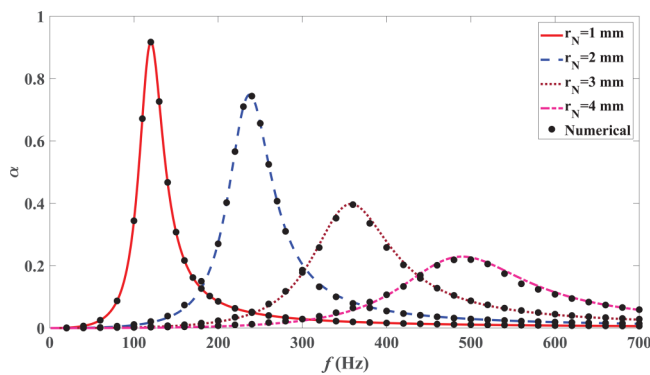


FIG. 3. A representative dataset of absorption coefficients for different frequencies created in the forward direction with electro-acoustic theory [refer to Eq. (5)]. Here, all the geometrical parameters are fixed ($l_N = 40$ mm, $l_C = 10$ mm, and $r_C = 10$ mm) except r_N . Markers denote numerical solutions for the same HRIN configurations.

the validity of the proposed electro-acoustic analogy, the absorption characteristics of HRIN are numerically assessed using COMSOL Multiphysics with a preset acoustic module. The numerical results obtained from the full field finite element simulations are compared with the analytical solutions and depicted in Fig. 3. Details of the numerical model are described in Appendix A. It is noticed that the absorption characteristics obtained through both approaches are in excellent agreement. Thus, by varying different geometric parameters, a large dataset is created through analytical estimation without much computational effort. The prepared datasets are rechecked several times in order to ensure their robustness and the dataset is noted to be free from errors and defects.

B. Inverse DNN architecture

A custom DNN model is proposed to validate the inverse prediction methodology. The schematic illustration of the proposed

DNN model is given in Fig. 4. It consists of an input layer, an output layer, and several hidden layers. Here, the absorption coefficients corresponding to frequencies ranging from 0 to 700 Hz are taken as the input while outputs are the geometrical parameters of the sound absorber. The hidden layers between the input and output layers learn the features and do intensive computations to establish the mapping between inputs and outputs. The proposed DNN consists of ten layers, which include 1D convolutional layers and dense layers. Convolutional layers are commonly used for analyzing spectral or time series data.^{59–62} It is noteworthy that 1D convolutional layers exhibited excellent performance in many applications^{63–65} and thereby it is chosen for the current settings.

A couple of 1D convolutional layers are used as initial layers, which learn the basic or simple features of input data. Those initial layers are followed by a flattened layer and seven dense layers. The flattened layer is used to flatten the output of the convolutional layer into a single long feature vector. This single feature vector is fed into the dense layers for extracting complex features (see Fig. 4). As the layers go deeper and deeper, the features that the architecture deals with become more complex. The number of neurons in each dense layer is hierarchically decreased from top to bottom and the number of neurons in the final layer is the same as that of output geometric parameters. The parameters of each layer used for reproducing the DNN model are detailed in Table II. More implementation details of DNN architecture are available in the previous works.^{66,67} The proposed DNN model is created and trained on Google Colaboratory platform of following specifications: 2.3 GHz Intel Xeon processor and NVIDIA Tesla K80 GPU with 12 GB RAM. Keras and Tensorflow 2.4.0 libraries compiled with custom Python scripts are used for deep learning algorithms. The proposed DNN model is trained and tested several times by optimizing the hyperparameters so as to minimize error.

C. Training and testing

The proposed DNN architecture is trained using the dataset generated and thereafter the geometric parameters of HRIN are predicted inversely. In this work, the frequency of interest is

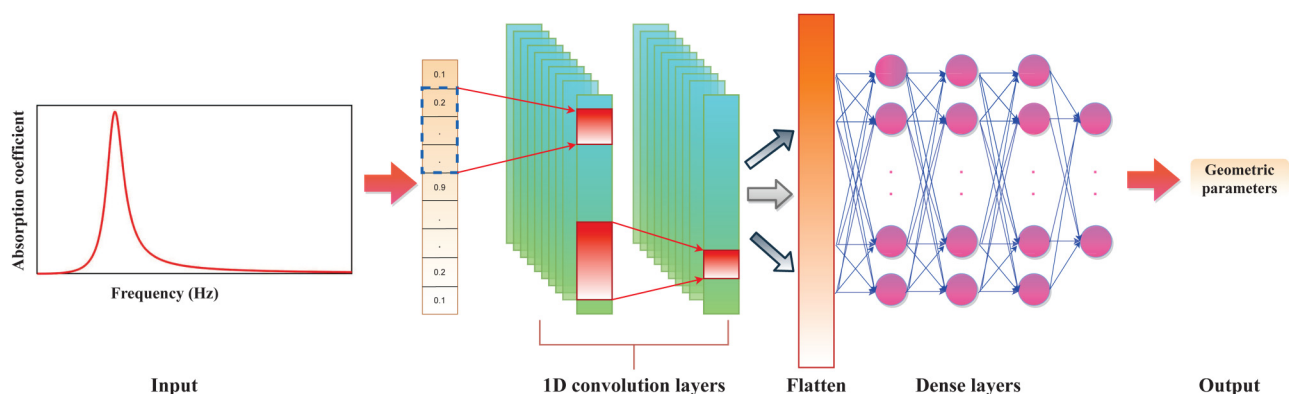


FIG. 4. Schematic illustration of the proposed DNN architecture for the prediction of geometric parameters from absorption characteristics. Absorption characteristics corresponding to the desired frequency regime are the input, while geometric parameters of the absorber are the outputs.

TABLE II. Details of constituent layer parameters of IDD model. Linear/rectified linear activation function (ReLU) are deployed for layer parameters.

No.	Layer name	Layer parameters	Output shape	Number of parameters
1	Conv 1D	64×10 , Strides = 1, Input shape = (701, 1), Activation = ReLU	692×64	704
2	Conv 1D	32×10 , Strides = 1, Activation = ReLU	683×32	20 512
3	Flattened	...	21 856	0
4	Dense	1024, Activation = ReLU	1 024	22 381 568
5	Dense	512, Activation = ReLU	512	524 800
6	Dense	256, Activation = ReLU	256	131 328
7	Dense	128, Activation = ReLU	128	32 896
8	Dense	64, Activation = ReLU	64	8 256
9	Dense	32, Activation = ReLU	32	2 080
10	Dense	3, Activation = Linear	3	99

0–700 Hz; hence, the proposed DNN model used absorption coefficients corresponding to this frequency regime as input. There are four defining geometric parameters associated with the design of HRIN. The prediction of these geometric parameters from absorption coefficients is a one to many mapping. Thus, it always leads to some error in prediction; hence, the inverse mapping does not always converge. To circumvent this difficulty, one geometrical parameter of HRIN is also fed into the network for accurately predicting the remaining three parameters. First, a DNN model (M1) is generated, which takes the cavity radius (r_C) as an input parameter and predicts the remaining three (l_N , l_C , and r_N) (see Table III). Note that the one-dimensional array of size (701, 1) with 700 absorption coefficients and one cavity radius is fed into the input layer of the M1 model. It then passes through the hierarchically ordered convolutional and dense layers and finally predicts the three geometrical parameters corresponding to the input absorption characteristics.

Initially, the influence of the data size on the performance of the DNN model (M1) is evaluated. Datasets with different sizes are

TABLE III. Performance of different DNN models of HRIN. For M1–M5 models, the absorption coefficient (α) corresponding to 0–700 Hz regime is given as inputs. All models except M5 are provided with a fixed geometrical parameter as additional input.

DNN model	Additional input parameter	Predicted parameters	Model performance	
			MAE (10^{-4})	MAPE (%)
M1	r_C	l_N, r_N, l_C	4.81	2.81
M2	r_N	l_N, l_C, r_C	9.87	4.78
M3	l_C	l_N, r_N, r_C	6.4	3.02
M4	l_N	l_C, r_N, r_C	2.25	1.78
M5	...	l_N, r_N, l_C, r_C	53.7	21.78

formed and the proposed DNN model is trained on each dataset separately. Further, individual datasets are segmented for training (80%) and validation (20%). In all the investigations detailed in this paper, the hyperparameters used are: learning rate = 0.0001, decay = 10^{-6} , batch size = 1000, and number of epochs = 500. Adam optimizer and mean absolute error loss function are selected to monitor the performance of the network. During the training phase, the overfitting problem is never encountered; hence, regularization techniques are not employed for this study. After the training process, the developed neural network model is tested on an unseen and mutually exclusive test set of 5000 samples. The performance of the DNN models is evaluated using the metrics, mean absolute error (MAE), and mean absolute percentage error (MAPE). These metrics are defined as

$$\text{MAE} = \frac{1}{n} \sum_{j=1}^n |y_j - \hat{y}_j| \quad (6)$$

and

$$\text{MAPE} = \frac{100}{n} \sum_{j=1}^n \frac{|y_j - \hat{y}_j|}{y_j} \%, \quad (7)$$

where y_j is the actual value, \hat{y}_j is the predicted value, and 'n' is the number of samples.

To choose a suitable sample size, the variation in error rate with the data size is estimated. From Fig. 5(a), it is evident that error reduces while the data size is increased. After a certain limit, there is no significant change in error rate and thereby the dataset is limited to 320 000 samples. The learning curve of the M1 model on this particular dataset is depicted in Fig. 5(b). The figure shows that the validation and training loss reduces considerably up to 200 epochs and thereafter they converge to a minimum value. The DNN model is further tested on a sample set of 64 000 to ensure the absence of overfitting. From these test data, 1000 samples are randomly chosen and the actual and predicted geometric parameters are marked in a parity plot (see Fig. 6). Here, the diagonal line represents the perfect correlation between the predicted and actual values. In most cases, all the three parameters are accurately predicted by the DNN model with MAE of 4.81×10^{-4} and MAPE of 2.81% as shown in Table III. This demonstrates that the proposed model is generalized and performs very well even on unseen data.

The final weights are obtained after training on the dataset having 320 000 samples for predicting the geometric parameters of HRIN. It is observed that the model accurately predicts the geometric parameters when these weights are used. To have an independent comparison, the absorption characteristics of HRIN modeled by Huang *et al.*²³ are given as an input to the IDD and geometric parameters of HRIN are computed inversely as shown in Table IV. Note that the maximum error in predicting one of the three dimensions is just 3.1%. Using the predicted values, the HRIN is analytically modeled and compared with the experimental results of Huang *et al.*²³ The comparison between the predicted result and that in the literature is given in Fig. 7. Within the frequency range of 100–200 Hz, the predicted absorption characteristics show good agreement with 2.3% average error in the absorption coefficient.

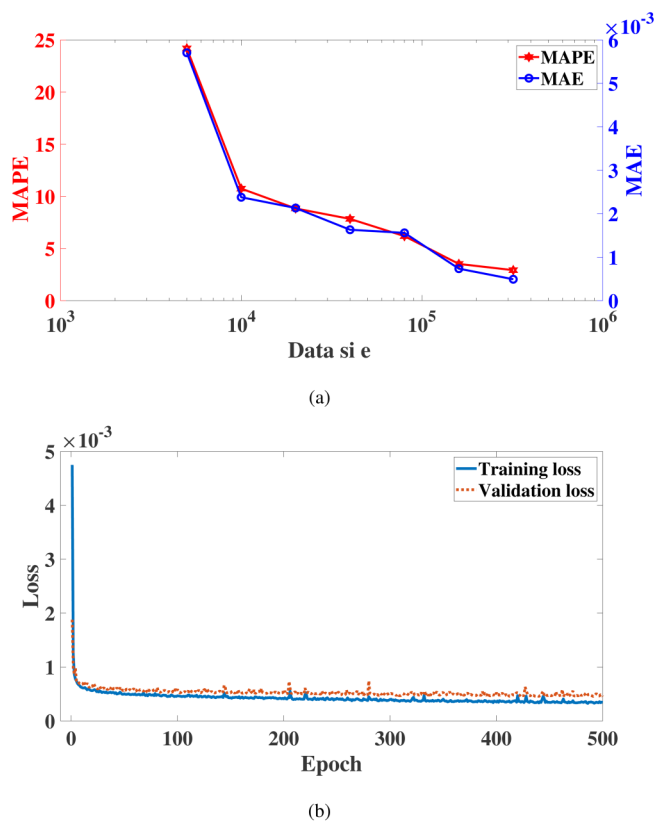


FIG. 5. Performance parameters of the IDDNN: (a) variation in error rate with logarithmic increase in the dataset, where the left axis shows the MAPE values and the right axis shows MAE values and (b) learning curves of the M1 model for training and validation on the dataset of 320 000 samples as functions of the training epochs.

Next, four more DNN models (M2–M5) are created to identify appropriate input parameters detailed in Table III. The first four DNN models (M1–M4) are generated by inputting one geometrical feature and predicting the remaining three. For all these cases, absorption coefficients corresponding to each frequency within the frequency range of 0–700 Hz along with one geometric parameter are fed into the DNN model to predict the remaining geometrical parameters. In contrast, for the last DNN model (M5), all the four parameters (l_N , l_C , r_C , and r_N) are predicted without any specific input. The M5 model is developed to understand the behavior of the DNN model when it is fed with absorption coefficients alone and without any prior knowledge about the geometry of HRIN. However, it is noticed that the M5 DNN model yielded high values of MAE and MAPE (see Table III), which proves its inefficiency in predicting the geometrical parameters of the absorber (HRIN) accurately. From the obtained performance characteristics given in Table III, it is evident that except M5 the remaining models perform satisfactorily, irrespective of the input geometric parameter. Thus, it is demonstrated that the IDDNN scheme can inversely predict the geometrical features of an

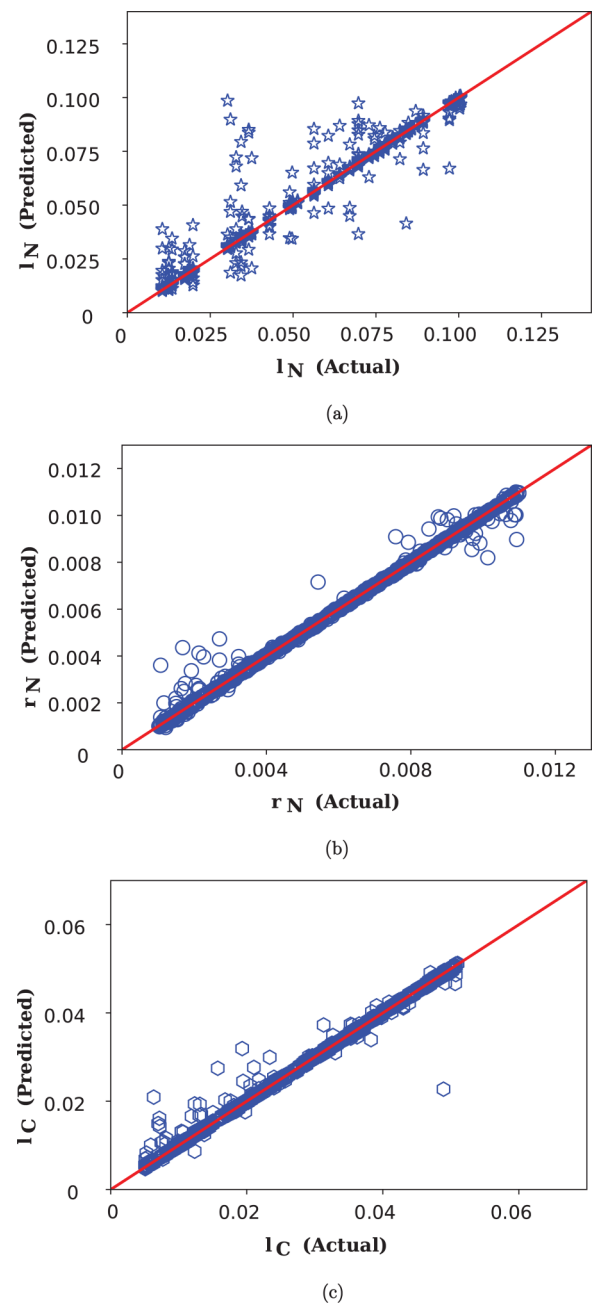


FIG. 6. Actual against predicted values of (a) neck length (l_N), (b) neck radius (r_N), and (c) cavity length (l_C) of 1000 samples of the HRIN dataset. The red diagonal line indicates the perfect correlation between the predicted and actual values. Predictions are done using the M1 DNN model.

HRIN absorber efficiently from input frequency response. From all these DNN models of HRIN, the M1 model in which the cavity radius is given as an input parameter along with absorption coefficients is chosen for detailed investigation. Indeed, the

TABLE IV. Predicted and actual geometric parameters of HRIN. For prediction using IDDN, the value of cavity radius (r_C) is given as an input along with the absorption coefficients (α) corresponding to the frequencies in the regime 0–700 Hz.

Parameters	Actual value (mm) ²³	Predicted value (IDDN) (mm)	Predicted value (GA) (mm)	Relative error (IDDN) (%)	Relative error (GA) (%)
l_N	40	39.42	44.82	1.45	12
r_N	1.75	1.735	1.87	0.85	7.78
l_C	10	10.31	9.10	3.1	9

cavity has the least influence on the formation of losses in a resonator.⁶⁸ In addition, the cavity radius, r_C , is considered as the least flexible design parameter when physically realizing a resonator based absorber.

In order to corroborate the superiority of the proposed IDDN scheme over conventional optimization techniques, a comparative analysis has been carried out. For this, the prediction of geometric parameters of HRIN is modeled as an optimization problem and it is solved using the genetic algorithm. The implementation details of GA are described in Appendix B. As given in Table IV, the design parameters predicted using genetic algorithm show a comparatively larger variation than that of IDDN predicted parameters. It is noteworthy that the maximum variation that occurred in predicting one of the three parameters (l_N) using GA is about 12%. From this, it is clear that IDDN has superior prediction capability than conventional techniques like genetic algorithms. The absorption characteristics obtained for HRIN from the geometric parameters predicted by GA and IDDN are compared with experimental results in Fig. 7. Within the frequency range of 100–200 Hz, the absorption coefficients predicted by GA exhibit an average variation of 5.1%, which is higher than that with IDDN predicted geometric parameters. Since an appropriate initial population is required, extending the GA technique

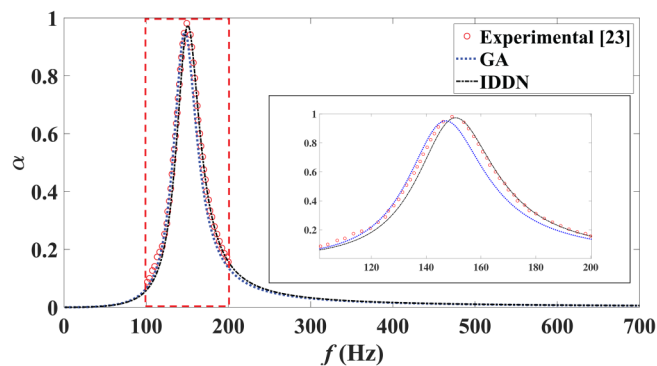


FIG. 7. Comparison of sound absorption characteristics of HRIN models, obtained from the geometric parameters predicted by GA and IDDN, with experimental results of Huang *et al.*²³ The magnified view of 100–200 Hz regime is given as inset.

to optimize a complex geometry is computationally intensive. From the current comparative analysis, it is evident that the proposed IDDN scheme is better to negotiate with complex geometries. Note that the previous findings by Sun *et al.*⁴⁶ also are in similar lines. Thus, the proposed IDDN strategy is applied to find out the optimum parameters of a complicated low-frequency acoustic absorber containing HR and MPP.

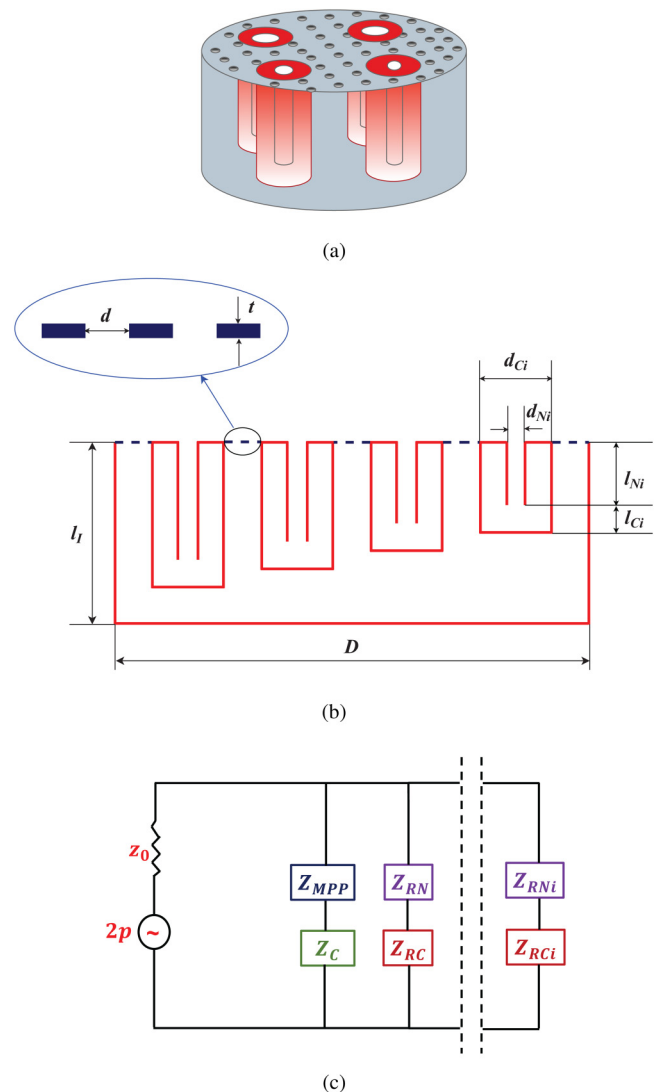


FIG. 8. (a) Physical model of P-MPPHR, (b) its schematic representation, where l_N is the neck length, l_C is the cavity beyond neck length, $r_N = d_N/2$ is the neck radius, and $r_C = d_C/2$ is the cavity radius of i th HRIN (i varies from 1 to 4). Further, d is the hole diameter, t is the thickness, and l_i is the cavity depth of MPP. (c) Equivalent electro-acoustic circuit, where Z_{RNi} is the acoustic impedance of the i th resonator neck, Z_{RCi} is the acoustic impedance of the i th resonator cavity, Z_{MPP} is the acoustic impedance of MPP, and Z_C is the acoustic impedance of MPP cavity.

TABLE V. Dimensions chosen for the dataset preparation for the prediction of geometrical parameters of P-MPPHR. Parameters kept as constant are thickness of the MPP $t = 1$ mm, porosity $\sigma = 1.4\%$, diameter of holes $d = 0.4$ mm, cavity depth $l_f = 70$ mm, $r_c = 15$ mm, and $l_c = 10$ mm.

Parameters	Limit of random values (mm)
$l_{N1}, l_{N2}, l_{N3}, l_{N4}$	30–50
$r_{N1}, r_{N2}, r_{N3}, r_{N4}$	3–6
D	90–130

III. INVERSE DESIGN OF LOW-FREQUENCY SOUND ABSORBER

The design of a low-frequency sound absorber with broad-band acoustic absorption characteristics and minimum thickness is a trending research problem in engineering acoustics. However, this objective is attempted in a previous analytical work,²⁷ where an absorber model is proposed in which parallel conjunction of MPP and multiple HRINs are used (P-MPPHR). The physical model of P-MPPHR is given in Fig. 8(a). Schematic representation of P-MPPHR model is depicted in Fig. 8(b), where all the relevant parameters are marked. It was observed that the P-MPPHR with four ($n = 4$) HRINs effectively absorbed sound in the low-mid frequency regime of 318–880 Hz.²⁷ In this model, all the four HRINs are arranged in a circular area having diameter D . However, optimization of geometrical parameters is a challenging task owing to the complexity in the geometry involved as well as the targeted low-frequency range. Here, the new inverse method is extended to accomplish optimum absorber parameters for the absorption of low-frequency sound waves. The dataset preparation and the training and testing of DNN for this particular absorber are detailed in Secs. III A and III B.

A. Dataset generation

To generate a sufficient amount of absorption data, the P-MPPHR model is analytically modeled based on electro-acoustic analogy. Here, the normal incidence sound absorption characteristics of the system are evaluated. The P-MPPHR model can be

TABLE VI. Dimensions of P-MPPHR sample models and corresponding resonance frequency of HRs used. f_i denotes the resonance frequency of i th HR. For all four samples $l_{M1} = 0.04$ m, $l_{C1} = 0.01$ m, $r_{C1} = 0.015$ m, $t = 0.001$ m, $\sigma = 1.4\%$, $d = 0.0004$ m, $D = 0.1$ m, and $l_f = 0.070$ m.

Absorber configuration	Geometrical parameters (dimensions in mm)	Resonance frequency of HRs (Hz)
A1	$r_{N1} = 3, r_{N2} = 3.5, r_{N3} = 4, r_{N4} = 4.5$	$f_1 = 233, f_2 = 272, f_3 = 310, f_4 = 350$
A2	$r_{N1} = 3.3, r_{N2} = 3.8, r_{N3} = 4.3, r_{N4} = 4.8$	$f_1 = 255, f_2 = 295, f_3 = 333, f_4 = 375$
A3	$r_{N1} = 3.6, r_{N2} = 4.1, r_{N3} = 4.6, r_{N4} = 5.1$	$f_1 = 280, f_2 = 318, f_3 = 358, f_4 = 399$
A4	$r_{N1} = 3.9, r_{N2} = 4.4, r_{N3} = 4.9, r_{N4} = 5.4$	$f_1 = 303, f_2 = 342, f_3 = 384, f_4 = 426$

considered as a locally reacting absorber where sound propagation is not possible in the direction parallel to an absorber surface.⁶⁹ Even though the absorber system is three-dimensional, it can be simplified into one-dimensional settings without loss of generality.⁷⁰ Thereby, the analytical formulation is one-dimensional for the current investigation.

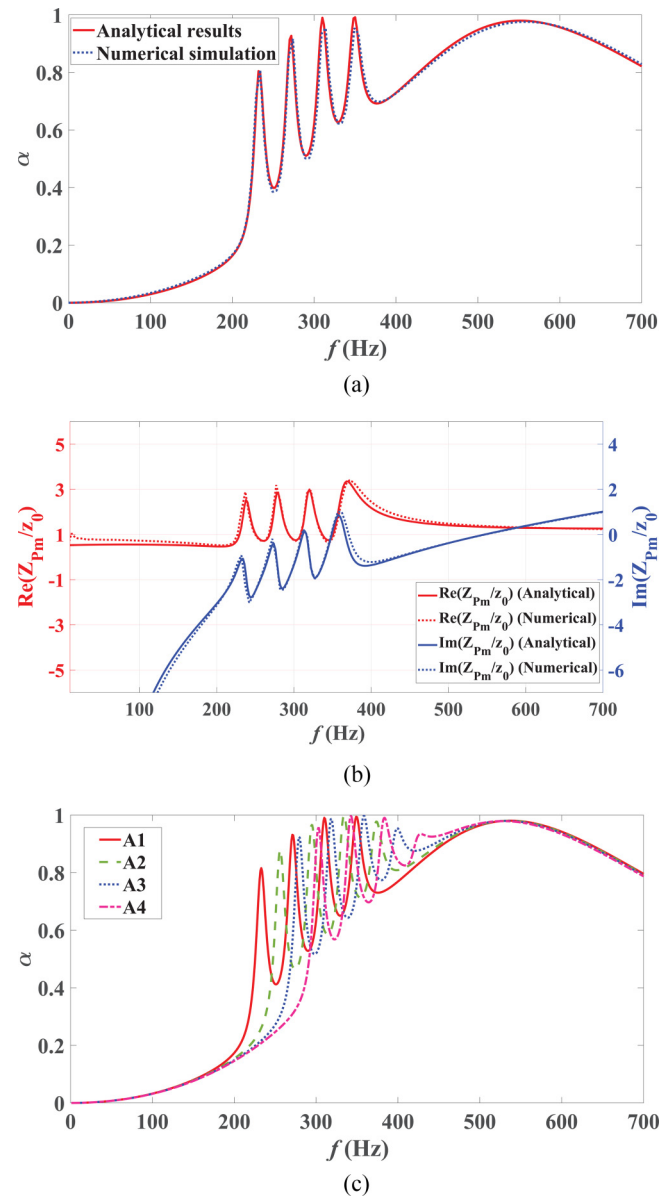


FIG. 9. Sample dataset created from electro-acoustic theory,²⁷ different P-MPPHR absorber samples (A1–A4) are obtained by varying dimensions as in Table VI. (a) Analytical estimation is compared against the computational results for A1 configuration. (b) Real and imaginary parts of the normalized impedance for A1 configuration. (c) Absorption coefficient against frequency for all the four configurations.

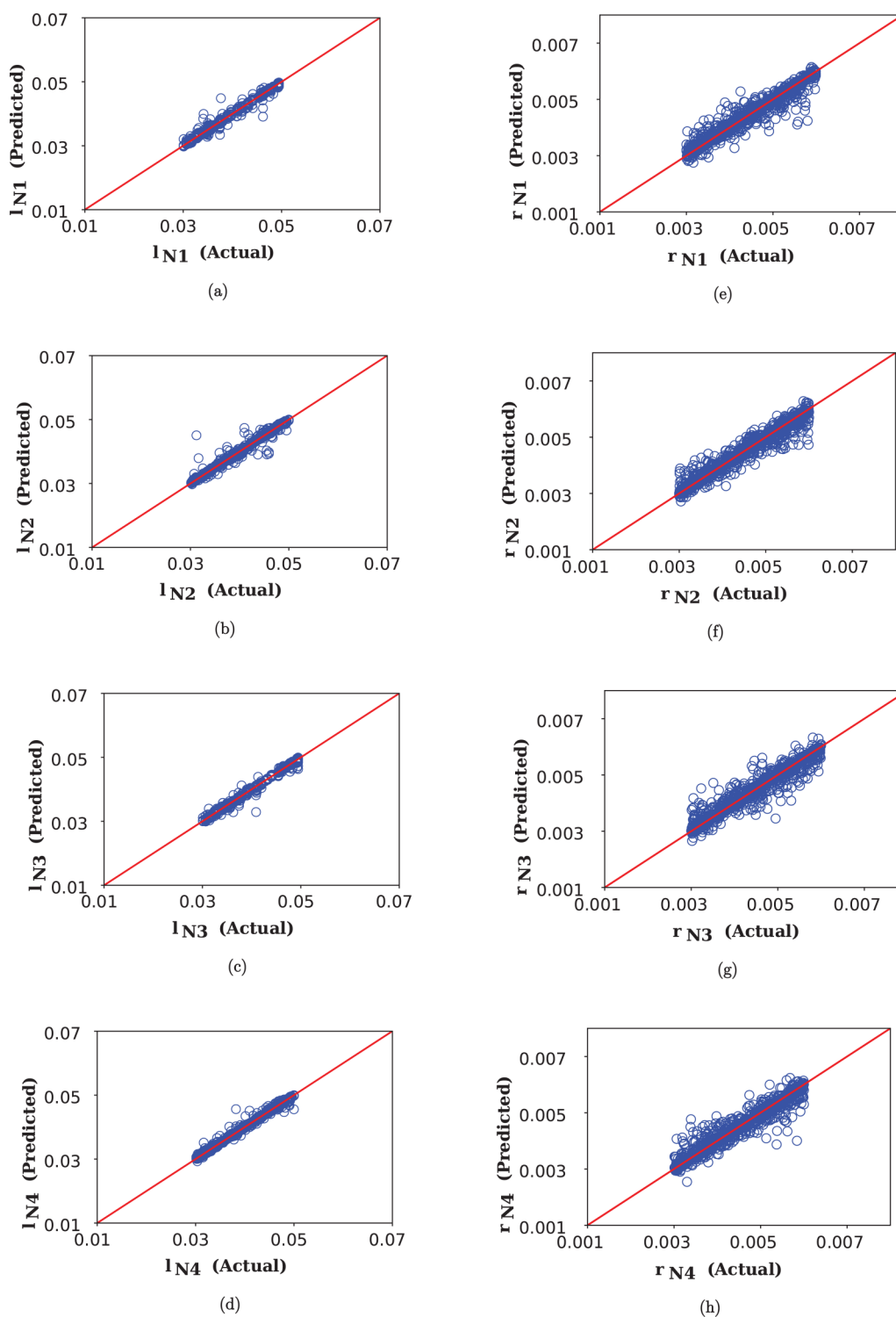


FIG. 10. Actual against predicted neck lengths (l_N) [(a)–(d)] and neck radii (r_N) [(e)–(h)] of 1000 samples of P-MPPHR dataset. The red diagonal indicates the perfect correlation between the predicted and actual values.

From equivalent electro-acoustic circuit [Fig. 8(c)], the specific acoustic impedance of P-MPPHR with “ n ” number of Helmholtz resonators (Z_{pm}) is given by²⁷

$$Z_{pm} = \frac{1}{\frac{S_m}{Z_{MPP} + Z_C} + \sum_{i=1}^n \frac{S_i}{Z_{HRI}}}, \quad (8)$$

where Z_{MPP} is the specific acoustic impedance of MPP and Z_C is the acoustic impedance of the backing cavity. Further, $S = A/(\pi D^2/4)$ is the area ratio of HR, where A is the area of HR and D is the diameter of P-MPPHR and $S_m = 1 - S$ is the area ratio of MPP. Further, the specific acoustic impedance of MPP $Z_{MPP} = z_0(R_{MPP} + jX_{MPP})$, where R_{MPP} and X_{MPP} are the normalized specific acoustic resistance and normalized specific acoustic reactance, respectively.¹² Furthermore, the normalized specific acoustic resistance and the normalized specific acoustic reactance¹² are

$$R_{MPP} = \frac{32t\eta}{\sigma\rho cd^2} \left(\sqrt{1 + \frac{k_m^2}{32}} + \frac{\sqrt{2}}{8} k_m \frac{d}{t} \right) \quad (9)$$

and

$$X_{MPP} = \frac{\omega t}{c\sigma} \left(1 + \frac{1}{\sqrt{9 + k_m^2/2}} + 0.85 \frac{d}{t} \right), \quad (10)$$

where t is plate thickness of MPP, d is the diameter of holes, and $k_m = (d/2)\sqrt{\rho\omega/\eta}$ is the perforate constant. Also, σ is the porosity of MPP, which is defined as the ratio of perforated area to the total area of the MPP. Thereafter, the acoustic impedance of backing cavity of MPP is estimated as

$$Z_C = -jz_0 \cot(kl_l), \quad (11)$$

where l_l is the length of the backing cavity of MPP. From that, Z_{pm} , the absorption coefficient of P-MPPHR, is obtained as

$$\alpha = 1 - \left| \frac{Z_{pm} - z_0}{Z_{pm} + z_0} \right|^2, \quad (12)$$

and it is used for the creation of the dataset by varying different influencing parameters. More details about the analytical procedure are available elsewhere.²⁷

During dataset generation, the following geometrical parameters of MPP are kept constant: thickness of the MPP $t = 1$ mm, porosity $\sigma = 1.4\%$, diameter of holes $d = 0.4$ mm, and cavity depth $l_l = 70$ mm. Also, for all four HRINs, r_C and l_C are fixed as 15 and 10 mm, respectively. Further, the neck length, l_{Ni} , and neck radii, r_{Ni} , of HRINs and the diameter of P-MPPHR, D are randomly varied to create different combinations of geometrical parameters. Index i corresponds to the number of HRIN, which assumes values from 1 to 4. The absorption characteristics corresponding to different combinations of these nine parameters (four l_{Ni} , four r_{Ni} , and D) are simulated using custom python scripts. In this case also, absorption coefficients corresponding to the

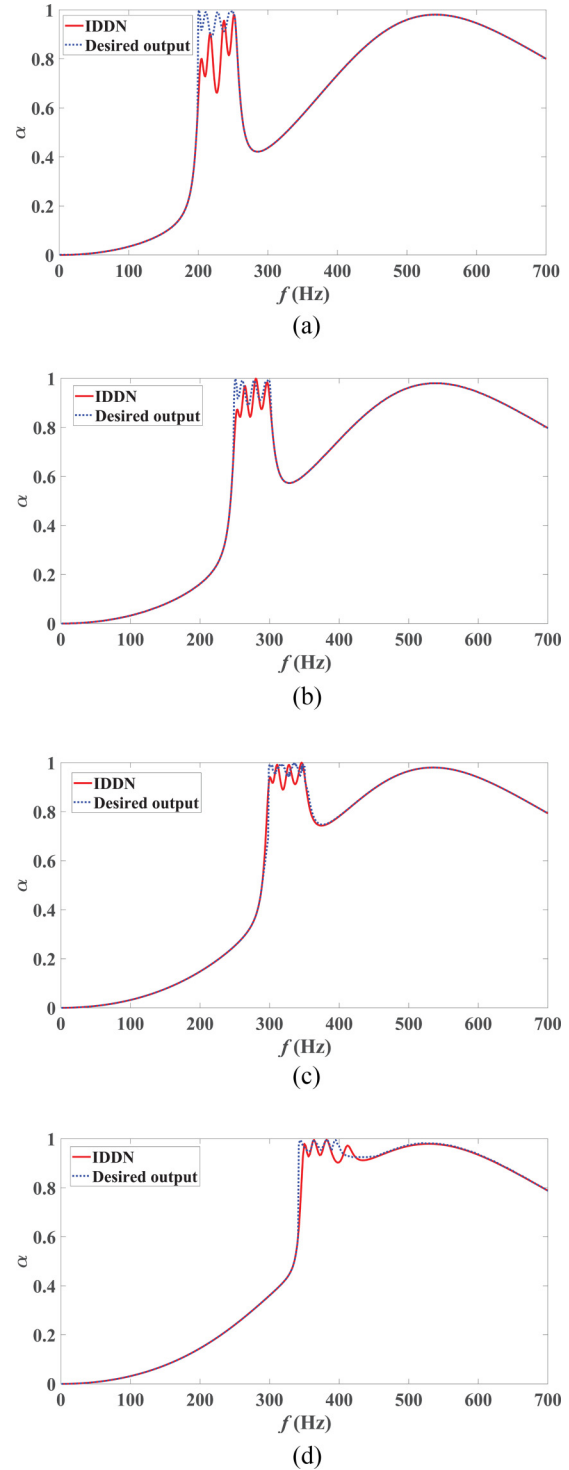


FIG. 11. Comparison between the desired absorption characteristics and the absorption characteristics generated using the IDDNN method for P-MPPHR models (a) P1, (b) P2, (c) P3, and (d) P4.

frequency regime 0–700 Hz are generated. The present study mainly focuses to predict the geometric parameters of a sound absorber, which has quasi-perfect absorption in the frequency range of 340–630 Hz. From previous works²⁷ and trial calculations, it is approximately estimated that the values of neck length and neck radius will be in the range 0.03–0.05 and 0.003–0.006 m, respectively, for the selected frequency regime. Hence, for dataset realization, random values in this range are chosen from a uniform distribution. Also, for containing the four HRINs of cavity radius 15 mm in the structure, it should have a minimum diameter of 90 mm. Therefore, for the diameter of P-MPPHR, random dimensions between 0.09 and 0.13 m are generated. For neck lengths and neck radii, the generated random values are rounded up to four significant digits while the diameter of MPP is rounded up to two significant digits. The dimensions chosen for the data preparation are detailed in Table V.

It is possible to create an infinite amount of data analytically by choosing different combinations of the nine parameters. However, 327 680 data samples are found to be sufficient enough to learn the relation between absorption characteristics and geometrical parameters. A sample dataset is generated from different P-MPPHR models obtained by selecting random geometrical features. For instance, models A1–A4 are produced from geometrical features provided in Table VI and Eq. (12) is deployed to obtain the frequency response. To corroborate the suitability of electro-acoustic theory, the frequency response of one of the configurations (A1) obtained from numerical and analytical predictions is plotted in Fig. 9(a) and is in good accord. As shown in Fig. 9(a), the absorption characteristics of the P-MPPHR absorber comprising of four Helmholtz resonators and a microperforated panel consist of five peak absorptions. Among them, the four narrow band peaks in the low-frequency regime correspond to the resonance condition of

the four Helmholtz resonators and the fifth one in the mid frequency regime (around 550 Hz) belongs to the MPP. For the better understanding of the loss mechanism, the impedance spectra of A1 model are plotted and are depicted in Fig. 9(b). In the impedance spectra, real (resistive) and imaginary (reactive) parts of the relative impedance of P-MPPHR model are plotted against frequency. At perfect absorption, the real part of normalized impedance is 1 and the imaginary part is 0. At that condition, the absorber shows impedance matching with the transmitting medium. However, this condition is often not strictly satisfied at low frequencies.^{24,26} Moreover, the acoustic characteristics of these representative models (A1–A4) are shown together in Fig. 9(c), which indeed shows that the bandwidths of frequency responses are different. The possibility of missing values or errors is counter checked to ensure its robustness. The generated dataset is divided into three categories as train, validation and test and each set contains 209 715, 52 429, and 65 536 samples, respectively. The presence of the dataset containing samples of desirable absorption characteristics is also checked. However, none of the samples in the entire dataset matched with the characteristics of the desired output. Hence, it is proven that the DNN model did not even see a single combination of geometrical parameters, which can produce the desired output. This totally nullified the chance of a biased dataset.

B. Inverse prediction of absorber parameters

Here, the DNN is used to map the relationship between the absorption characteristics and the eight geometrical parameters of the absorber. Hence, the output of the problem is the predicted values of neck lengths and neck radii of four HRINs. For this, the proposed DNN is slightly modified. As the output of the DNN consists of eight

TABLE VII. Predicted geometrical parameters of sample P-MPPHR models. For predicting geometric features of P-MPPHR, D is given as an input along with the absorption coefficients (α) corresponding to 0–700 Hz regime. For all sample data, $l_{ci} = 0.01$ m, $r_{ci} = 0.015$ m, $t = 0.001$ m, $\sigma = 1.4\%$, $d = 0.0004$ m, $D = 0.1$ m, and $l_i = 0.070$ m.

Desired feature	Dimensions of predicted geometrical parameters (mm)	Resonance frequency of HRs (Hz)	Average relative error between the desired and obtained absorption characteristics (%)
(P1) 90% absorption in the frequency range of 200–250 Hz	$l_{N1} = 48, l_{N2} = 46.7,$ $l_{N3} = 48.5, l_{N4} = 48.5$ $r_{N1} = 3.8, r_{N2} = 3,$ $r_{N3} = 3.3, r_{N4} = 3.6$	$f_1 = 204, f_2 = 218$ $f_3 = 238, f_4 = 251$	3.47
(P2) 90% absorption in the frequency range of 250–300 Hz	$l_{N1} = 49.2, l_{N2} = 44.1,$ $l_{N3} = 42.1, l_{N4} = 35.7$ $r_{N1} = 4.3, r_{N2} = 3.7,$ $r_{N3} = 3.4, r_{N4} = 3.5$	$f_1 = 254, f_2 = 264$ $f_3 = 281, f_4 = 297$	1.18
(P3) 90% absorption in the frequency range of 300–350 Hz	$l_{N1} = 32.6, l_{N2} = 45.6,$ $l_{N3} = 38.8, l_{N4} = 44.5$ $r_{N1} = 3.8, r_{N2} = 4.3,$ $r_{N3} = 3.9, r_{N4} = 4.6$	$f_1 = 300, f_2 = 311$ $f_3 = 327, f_4 = 345$	0.43
(P4) 90% absorption in the frequency range of 340–630 Hz	$l_{N1} = 30.7, l_{N2} = 31,$ $l_{N3} = 48.2, l_{N4} = 31$ $r_{N1} = 4.3, r_{N2} = 4,$ $r_{N3} = 5.2, r_{N4} = 3.8$	$f_1 = 350, f_2 = 364$ $f_3 = 382, f_4 = 412$	0.58

parameters, the final layer has eight neurons, also an additional dense layer of 1024 neurons is added after the flattened layer to improve the performance. All other layer parameters are the same as that of HRIN discussed in Sec. II B and Table II. Also, the hyperparameters, optimizer, and loss function used in this prediction process are same as that of the HRIN case (refer to Sec. II C). The input of the model is a one-dimensional array of size (701, 1), and it includes 700 absorption coefficients and the diameter of P-MPPHR. Giving the diameter of P-MPPHR as an additional input to the DNN certainly reduces the difficulty of one to many mapping. Hence, the model converges into an optimum solution much faster. The inputs pass through the hierarchically ordered convolutional and dense layers and finally predict the eight geometrical parameters corresponding to the input absorption characteristics. The modified DNN performed well on train data as well as the validation data. Thus, in validation dataset, MAE of 1.62×10^{-4} and MAPE of 1.87% are obtained. Thereafter the model is tested on an unseen and mutually exclusive dataset of 65 536 samples for evaluating the performance. In these test data, MAE of 1.75×10^{-4} and MAPE of 1.98% are obtained. From the test data, 1000 samples are randomly chosen and the predicted and actual values of the eight geometric parameters are plotted as in Fig. 10. In all cases, the predicted and actual values are in good agreement. Hence, the performance of DNN is found to be quite good to predict the geometrical parameters of the P-MPPHR model.

After successful training and testing, various desired output frequency signals are fed to the IDDN to inversely calculate geometric parameters. A P-MPPHR with four HRINs yields four resonance peaks in the low-frequency regime and a peak in the mid frequency region.²⁷ For instance, the four such absorption characteristics (blue dotted lines of Fig. 11) are generated randomly (P1–P4) and passed through the inverse neural network. In addition to the absorption coefficient data, the diameter of the P-MPPHR is also fed. For these four cases, D is given as 100 mm. These signals (P1–P4) are used to estimate the geometrical features of the absorber. Further, the geometry obtained from the inverse predictions is employed to recreate the frequency response shown in Figs. 11(a)–11(d) (red solid lines). The predicted geometric parameters of HRINs are shown in Table VII. Note that the desired output and obtained frequency responses are in good agreement and the average error is very low as evident from Table VII. To further investigate the acoustic properties of these models (P1–P4), the impedance spectra are generated and plotted in Figs. 12(a)–12(d). In the impedance spectra, the resistive and the reactive parts of normalized impedance are plotted against frequency. Note that, at perfect absorption condition, the resistive part of the impedance is 1 and the imaginary part is 0.

Among the above-mentioned four absorbers, the one having quasi-perfect absorption in the frequency range of 340–630 Hz (P4) requires special attention owing to its broadband absorption characteristics. In Fig. 11(d), the desired absorption characteristics and absorption characteristics generated using the IDDN method are compared for P4. The P-MPPHR model (P4) with predicted dimensions exhibited more than 90% absorption in the frequency range of 347–630 Hz. Hence, the proposed methodology is successfully implemented to develop a quasi-perfect absorber in the low-mid frequency regime. The proposed P-MPPHR model has quasi-perfect sound absorption over two 1/3 octave bands. Further, the total thickness of this model is 7 cm only, which is indeed sub-

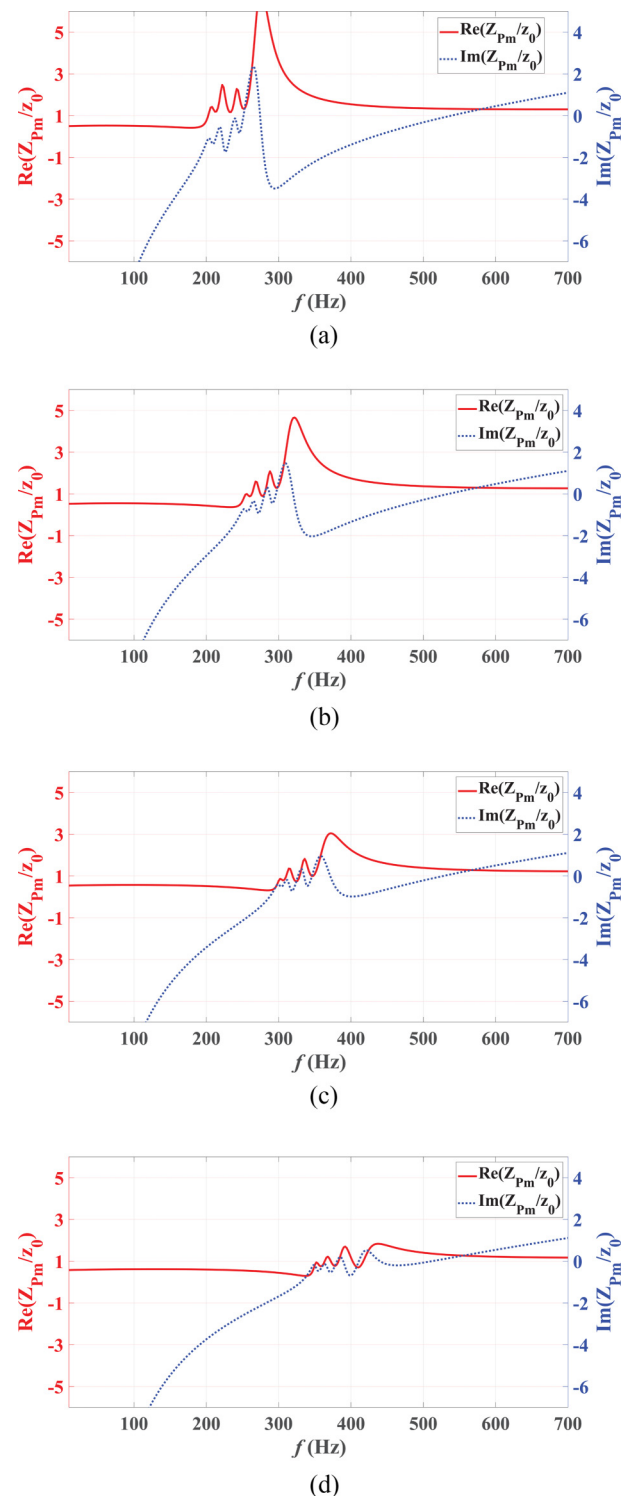


FIG. 12. The real and imaginary parts of the normalized impedance for P-MPPHR models (a) P1, (b) P2, (c) P3, and (d) P4.

wavelength in scale. Thereby, the IDNN scheme exhibited excellent performance in the inverse prediction of geometrical dimensions of an absorber for a desired acoustic signal. Most importantly, this novel strategy can effortlessly be extended to inversely predict the geometrical features of much complex acoustic structures such as superlenses, phononic crystals, labyrinthine, cloaking devices, etc., by generating required datasets using theoretical/experimental means. These acoustic structures can effortlessly be fabricated using advanced manufacturing procedures such as selective laser sintering, fused filament fabrication, powder metallurgy, and so on.

The IDNN technique is a well-posed inverse methodology and it consistently provides feasible and realistic solutions with high fidelity. Further, the proposed methodology is capable of doing intrusively complex parallel computations with a faster convergence rate. The deep learning techniques adopted for the IDNN methodology are better than the conventional evolution or gradient based optimization techniques. It successfully identifies the desirable features of the dataset and perfectly acquires optimal solutions without being trapped in local minima or saddle points, which implies the robustness of this strategy. A comparative analysis with the genetic algorithm, carried out in this study, corroborates the prediction efficiency and computational efficiency of the IDNN scheme. Currently, the DNN works in a brute force way, without taking the physical insights of the real life problems. By coupling the DNN with physical laws, such limitations are expected to be solved without compromising the performance. Thereby, expanding the IDNN method by coupling DNN with governing physical laws is a pertinent research problem under investigation.

IV. CONCLUSIONS

In this study, an inverse method for predicting the geometrical parameters of a sound absorber from its absorption characteristics using the deep neural network is presented. For that, a novel deep learning architecture is designed, trained, and successfully tested. The developed neural network consists of hierarchically ordered convolutional and dense layers and its hyperparameters are fine tuned to obtain maximum efficiency. Absorption coefficients corresponding to the frequencies ranging from 0 to 700 Hz are taken as the inputs and geometric parameters of the sound absorber are produced as the outputs. The dataset required for the training and testing is developed using electro-acoustic theory. To corroborate the electro-acoustic theory, full field finite element simulations are carried out. Initially, the proposed IDNN method is implemented on a standard sound absorber based on HR. Later, the study is extended to design a quasi-perfect absorber, which is a combination of MPP and HRIN for broadband absorption. Optimum geometrical dimensions of a P-MPPHR model are predicted using IDNN. The major conclusions of the examination are given below:

- The proposed IDNN method is an effective strategy to inversely design acoustic absorbers of desirable functionalities and it can be considered as an alternative strategy for conventional optimization or inverse techniques.
- The IDNN method is successfully implemented on an existing absorber (HRIN) with high accuracy and faster performance. The predicted geometrical parameters of HRIN showed less than 3% variation with the reported values.

- The influence of dataset size on the performance of the IDNN method is evaluated and it showed that the performance of IDNN increases with dataset size up to a certain limit.
- Using the novel IDNN method, a low-mid frequency sound absorber comprising parallel combination of MPP and multiple HRINs is inversely designed from desired absorption characteristics. The designed absorber exhibited quasi-perfect absorption in the frequency regime of 347–630 Hz with an effective absorption bandwidth that extended to more than two 1/3 octave bands.

However, the choice of neural network architecture and the selection of hyperparameters need further investigations for further improvement of efficiency. As a future work, the prediction of design parameters of different acoustic absorbers can be encompassed to a single neural network through transfer learning methods. Further, in unsupervised networks such as autoencoders, generative adversarial networks are expected to improve the performance of the proposed strategy and are under investigation. Moreover, the proposed inverse prediction method discussed in this paper is expected to have wide applications in engineering design in general and acoustics in particular. Once a dataset is available through experiment/theory, this method can be deployed to design any type of sound absorber with desirable absorption characteristics.

ACKNOWLEDGMENTS

One of the authors (K. Mahesh) gratefully acknowledges the research sponsorship under the AICTE Doctoral Fellowship (Government of India) scheme.

APPENDIX A: NUMERICAL MODEL

In this work, the full field finite element simulations are carried out using COMSOL multiphysics software. An impedance tube containing the absorber is considered for simulations. The acoustic fields inside the impedance tube are governed by the Helmholtz equation of the form⁷¹

$$\Delta p + k^2 p = 0, \quad (\text{A1})$$

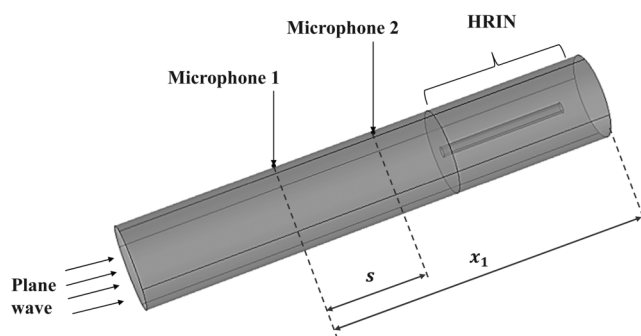


FIG. 13. Numerical model of the impedance tube setup with HRIN.

TABLE VIII. Parameters of the JCA model for circular cross section of radius r in terms of dynamic viscosity η of the fluid medium.

Geometry	Viscous characteristics length Λ	Thermal characteristics length Λ'	Tortuosity α_∞	Static flow resistivity σ	Open porosity ϕ
Neck	r	r	1	$\frac{8\eta}{\phi r^2}$	1

where $k = \omega/c$ is the wave number and p is the acoustic pressure. The wave number is defined by the angular frequency ω and the velocity of sound c of the medium.

The numerical model of HRIN inside an impedance tube is given in Fig. 13. Sound hard boundary conditions are imposed on the walls. A normal incident plane wave of magnitude 1 Pa is impinging from the left end of the impedance tube, where matched boundary condition is incorporated. The transmitting fluid medium inside the impedance tube is chosen as air with density $\rho = 1.16\text{ kg/m}^3$ and velocity of sound $c = 346\text{ m/s}$. The domain inside the resonator neck is modeled as equivalent fluid using complex effective density and effective bulk modulus determined using the Johnson–Champoux–Allard (JCA) model.⁷² The JCA parameters used for the modeling are given in Table VIII. While designing MPP, the interior perforated plate condition is chosen. For a simplified modeling approach, the fluid structure interactions and non-linear effects are not considered. The pressure response (p_1 and p_2) at two points, which corresponds to the microphone positions, is extracted for analysis. If first and second microphones are separated from absorber by the distances of x_1 and x_2 , respectively, then the transfer function H_{12} can be formulated as

$$H_{12} = \frac{p_2}{p_1} = \frac{e^{ikx_2} + Re^{-ikx_2}}{e^{ikx_1} + Re^{-ikx_1}}, \quad (\text{A2})$$

where s is the distance between the microphones. Then, from H_{12} , the reflection coefficient (R) is calculated as

$$R = \frac{H_{12} - e^{-iks}}{e^{iks} - H_{12}} e^{2ikx_1}, \quad (\text{A3})$$

and the absorption coefficient (α) as

$$\alpha = 1 - |R|^2. \quad (\text{A4})$$

APPENDIX B: DETAILS OF GENETIC ALGORITHM

GA is an evolutionary optimization technique, which is based on the mechanics of natural selection and natural genetics. In this technique, the algorithm repeatedly modifies a population of individual solutions. At each step, GA selects random individuals from the old population and uses them as parents to generate new offspring.^{30,73} Here, the MATLAB genetic algorithm toolbox is used for the optimization process. The prediction of geometric parameters of the HRIN is modeled as an optimization problem and it is solved using the genetic algorithm. The experimental results of the model showed almost perfect absorption at 149 Hz and hence the algorithm is modeled such that the objective of the optimization is chosen as to maximize the absorption at 149 Hz.

The objective function is to maximize the absorption coefficient at 149 Hz,

$$F = \max(\alpha_{f=149\text{ Hz}}),$$

subject to the constraints:

- $10\text{ mm} \leq l_N \leq 100\text{ mm}$,
- $1\text{ mm} \leq r_N \leq 10\text{ mm}$, and
- $5\text{ mm} \leq l_C \leq 50\text{ mm}$.

For the above constraints, the design variables l_N , r_N , and l_C are optimized. The parameters selected for the GA are the following:

- population size: 200,
- crossover rate: 0.9,
- elite count: 20,
- selection type: Roulette type, and
- crossover type: single point crossover.

DATA AVAILABILITY

The data that support the findings of this study are available from the corresponding author upon reasonable request.

REFERENCES

- ¹I. van Kamp and F. van den Berg, "Health effects related to wind turbine sound, including low-frequency sound and infrasound," *Acoust. Aust.* **46**, 31–57 (2018).
- ²C. Roberts, "Low frequency noise from transportation sources," in *Proceedings of the 20th International Congress on Acoustics, Sydney, Australia* (International Congress on Acoustics, 2010), pp. 23–27.
- ³H. G. Leventhall, "Low frequency noise and annoyance," *Noise Health* **6**, 59–72 (2004), available at <https://www.noiseandhealth.org/text.asp?2004/6/23/59/31663>.
- ⁴K. Waye, "Effects of low frequency noise and vibrations: Environmental and occupational perspectives," in *Encyclopedia of Environmental Health*, edited by J. Nriagu (Elsevier, Burlington, 2011), pp. 240–253.
- ⁵B. Berglund, P. Hassmen, and R. S. Job, "Sources and effects of low-frequency noise," *J. Acoust. Soc. Am.* **99**, 2985–3002 (1996).
- ⁶V. Tyagi, K. Kumar, and V. K. Jain, "A study of the spectral characteristics of traffic noise attenuation by vegetation belts in Delhi," *Appl. Acoust.* **67**, 926–935 (2006).
- ⁷I. Ekici and H. Bougdah, "A review of research on environmental noise barriers," *Build. Acoust.* **10**, 289–323 (2003).
- ⁸X. Tang and X. Yan, "Acoustic energy absorption properties of fibrous materials: A review," *Compos. Part A: Appl. Sci. Manuf.* **101**, 360–380 (2017).
- ⁹U. Ingard, "On the theory and design of acoustic resonators," *J. Acoust. Soc. Am.* **25**, 1037–1061 (1953).
- ¹⁰R. Prydz, L. Wirt, H. Kuntz, and L. Pope, "Transmission loss of a multilayer panel with internal tuned Helmholtz resonators," *J. Acoust. Soc. Am.* **87**, 1597–1602 (1990).

- ¹¹S. Kim, Y. H. Kim, and J. H. Jang, "A theoretical model to predict the low-frequency sound absorption of a Helmholtz resonator array," *J. Acoust. Soc. Am.* **119**, 1933–1936 (2006).
- ¹²D.-Y. Maa, "Theory and design of microperforated panel sound-absorbing constructions," *Sci. Sin.* **18**, 55–71 (1975), available at <https://www.sciengine.com/publisher/scp/journal/Math%20A0/18/1/10.1360/ya1975-18-1-55?slug=fulltext#>.
- ¹³D.-Y. Maa, "Microperforated-panel wideband absorbers," *Noise Control Eng. J.* **29**, 77 (1987).
- ¹⁴D.-Y. Maa, "Potential of microperforated panel absorber," *J. Acoust. Soc. Am.* **104**, 2861–2866 (1998).
- ¹⁵K. Sakagami, Y. Nagayama, M. Morimoto, and M. Yairi, "Pilot study on wide-band sound absorber obtained by combination of two different microperforated panel (MPP) absorbers," *Acoust. Sci. Technol.* **30**, 154–156 (2009).
- ¹⁶X. Li, Q. Wu, L. Kang, and B. Liu, "Design of multiple parallel-arranged perforated panel absorbers for low frequency sound absorption," *Materials* **12**, 2099 (2019).
- ¹⁷C. Wang, L. Cheng, J. Pan, and G. Yu, "Sound absorption of a micro-perforated panel backed by an irregular-shaped cavity," *J. Acoust. Soc. Am.* **127**, 238–246 (2010).
- ¹⁸C. Wang and L. Huang, "On the acoustic properties of parallel arrangement of multiple micro-perforated panel absorbers with different cavity depths," *J. Acoust. Soc. Am.* **130**, 208–218 (2011).
- ¹⁹X. Shi and C. M. Mak, "Helmholtz resonator with a spiral neck," *Appl. Acoust.* **99**, 68–71 (2015).
- ²⁰S. Tang, "On Helmholtz resonators with tapered necks," *J. Sound Vib.* **279**, 1085–1096 (2005).
- ²¹A. Selamet and I. Lee, "Helmholtz resonator with extended neck," *J. Acoust. Soc. Am.* **113**, 1975–1985 (2003).
- ²²C. Cai, C.-M. Mak, and X. Shi, "An extended neck versus a spiral neck of the Helmholtz resonator," *Appl. Acoust.* **115**, 74–80 (2017).
- ²³S. Huang, X. Fang, X. Wang, B. Assouar, Q. Cheng, and Y. Li, "Acoustic perfect absorbers via Helmholtz resonators with embedded apertures," *J. Acoust. Soc. Am.* **145**, 254–262 (2019).
- ²⁴J. Guo, Y. Fang, Z. Jiang, and X. Zhang, "Acoustic characterizations of Helmholtz resonators with extended necks and their checkerboard combination for sound absorption," *J. Phys. D: Appl. Phys.* **53**, 505504 (2020).
- ²⁵J. Guo, X. Zhang, Y. Fang, and Z. Jiang, "A compact low-frequency sound-absorbing metasurface constructed by resonator with embedded spiral neck," *Appl. Phys. Lett.* **117**, 221902 (2020).
- ²⁶M. Duan, C. Yu, Z. Xu, F. Xin, and T. J. Lu, "Acoustic impedance regulation of Helmholtz resonators for perfect sound absorption via roughened embedded necks," *Appl. Phys. Lett.* **117**, 151904 (2020).
- ²⁷K. Mahesh and R. S. Mini, "Theoretical investigation on the acoustic performance of Helmholtz resonator integrated microperforated panel absorber," *Appl. Acoust.* **178**, 108012 (2021).
- ²⁸J. Peurifoy, Y. Shen, L. Jing, Y. Yang, F. Cano-Renteria, B. G. DeLacy, J. D. Joannopoulos, M. Tegmark, and M. Soljačić, "Nanophotonic particle simulation and inverse design using artificial neural networks," *Sci. Adv.* **4**, eaar4206 (2018).
- ²⁹Z. Liu, D. Zhu, S. P. Rodrigues, K.-T. Lee, and W. Cai, "Generative model for the inverse design of metasurfaces," *Nano Lett.* **18**, 6570–6576 (2018).
- ³⁰D. E. Goldberg and J. H. Holland, *Genetic Algorithms and Machine Learning* (Kluwer Academic Publishers, 1988).
- ³¹D. Liu, Y. Tan, E. Khoram, and Z. Yu, "Training deep neural networks for the inverse design of nanophotonic structures," *ACS Photonics* **5**, 1365–1369 (2018).
- ³²P. Chen, C. Chen, H. Wang, J. Tsai, and W.-X. Ni, "Synthesis design of artificial magnetic metamaterials using a genetic algorithm," *Opt. Express* **16**, 12806–12818 (2008).
- ³³Z. Lin, B. Grover, F. Capasso, A. W. Rodriguez, and M. Lončar, "Topology-optimized multilayered metaoptics," *Phys. Rev. Appl.* **9**, 044030 (2018).
- ³⁴S. Goudos and J. Sahalos, "Microwave absorber optimal design using multi-objective particle swarm optimization," *Microw. Opt. Technol. Lett.* **48**, 1553–1558 (2006).
- ³⁵C. Y. Kao, S. Osher, and E. Yablonovitch, "Maximizing band gaps in two-dimensional photonic crystals by using level set methods," *Appl. Phys. B* **81**, 235–244 (2005).
- ³⁶J. Hou, H. Lin, W. Xu, Y. Tian, Y. Wang, X. Shi, F. Deng, and L. Chen, "Customized inverse design of metamaterial absorber based on target-driven deep learning method," *IEEE Access* **8**, 211849–211859 (2020).
- ³⁷E. S. Harper, E. J. Coyle, J. P. Vernon, and M. S. Mills, "Inverse design of broadband highly reflective metasurfaces using neural networks," *Phys. Rev. B* **101**, 195104 (2020).
- ³⁸N. Gao, B. Wang, K. Lu, and H. Hou, "Teaching-learning-based optimization of an ultra-broadband parallel sound absorber," *Appl. Acoust.* **178**, 107969 (2021).
- ³⁹X. Chen, Z. Wei, M. Li, and P. Rocca, "A review of deep learning approaches for inverse scattering problems (invited review)," *Prog. Electromagnet. Res.* **167**, 67–81 (2020).
- ⁴⁰M. S. Hossain, Z. C. Ong, Z. Ismail, S. Noroozi, and S. Y. Khoo, "Artificial neural networks for vibration based inverse parametric identifications: A review," *Appl. Soft Comput.* **52**, 203–219 (2017).
- ⁴¹M. T. McCann, K. H. Jin, and M. Unser, "Convolutional neural networks for inverse problems in imaging: A review," *IEEE Signal Process. Mag.* **34**, 85–95 (2017).
- ⁴²Y. Mao, X. Guo, and Y. Zhao, "A state space force identification method based on Markov parameters precise computation and regularization technique," *J. Sound Vib.* **329**, 3008–3019 (2010).
- ⁴³S.-J. Kim and S.-K. Lee, "Experimental identification for inverse problem of a mechanical system with a non-minimum phase based on singular value decomposition," *J. Mech. Sci. Technol.* **22**, 1504–1509 (2008).
- ⁴⁴C. Budd, M. A. Freitag, and N. Nichols, "Regularization techniques for ill-posed inverse problems in data assimilation," *Comput. Fluids* **46**, 168–173 (2011).
- ⁴⁵K. C. Giannakoglou and D. I. Papadimitriou, "Adjoint methods for shape optimization," in *Optimization and Computational Fluid Dynamics* (Springer, 2008), pp. 79–108.
- ⁴⁶X. Sun, H. Jia, Y. Yang, H. Zhao, Y. Bi, Z. Sun, and J. Yang, "Acoustic structure inverse design and optimization using deep learning," *arXiv:2102.02063* (2021).
- ⁴⁷W. W. Ahmed, M. Farhat, X. Zhang, and Y. Wu, "Deterministic and probabilistic deep learning models for inverse design of broadband acoustic cloak," *arXiv:2010.14866* (2020).
- ⁴⁸I. Goodfellow, Y. Bengio, A. Courville, and Y. Bengio, *Deep Learning* (MIT Press, Cambridge, 2016), Vol. 1.
- ⁴⁹G. Ciaburro, G. Iannace, J. Passaro, A. Bifulco, D. Marano, M. Guida, F. Marulo, and F. Branda, "Artificial neural network-based models for predicting the sound absorption coefficient of electrospun poly (vinyl pyrrolidone)/silica composite," *Appl. Acoust.* **169**, 107472 (2020).
- ⁵⁰J. H. Jeon, S. S. Yang, and Y. J. Kang, "Estimation of sound absorption coefficient of layered fibrous material using artificial neural networks," *Appl. Acoust.* **169**, 107476 (2020).
- ⁵¹G. Iannace, G. Ciaburro, and A. Trematerra, "Modelling sound absorption properties of broom fibers using artificial neural networks," *Appl. Acoust.* **163**, 107239 (2020).
- ⁵²X. Huang, H. Huang, J. Wu, M. Yang, and W. Ding, "Sound quality prediction and improving of vehicle interior noise based on deep convolutional neural networks," *Expert Syst. Appl.* **160**, 113657 (2020).
- ⁵³M. H. Tahersima, K. Kojima, T. Koike-Akino, D. Jha, B. Wang, C. Lin, and K. Parsons, "Deep neural network inverse design of integrated photonic power splitters," *Sci. Rep.* **9**, 1368 (2019).
- ⁵⁴L. Piloizzi, F. A. Farrelly, G. Marcucci, and C. Conti, "Machine learning inverse problem for topological photonics," *Commun. Phys.* **1**, 57 (2018).
- ⁵⁵J. Ma, Y. Huang, M. Pu, D. Xu, J. Luo, Y. Guo, and X. Luo, "Inverse design of broadband metasurface absorber based on convolutional autoencoder network and inverse design network," *J. Phys. D: Appl. Phys.* **53**, 464002 (2020).

- ⁵⁶V. Sekar, M. Zhang, C. Shu, and B. C. Khoo, "Inverse design of airfoil using a deep convolutional neural network," *AIAA J.* **57**, 993–1003 (2019).
- ⁵⁷B. Zheng, J. Yang, B. Liang, and J.-C. Cheng, "Inverse design of acoustic meta-materials based on machine learning using a Gauss-Bayesian model," *J. Appl. Phys.* **128**, 134902 (2020).
- ⁵⁸S.-H. Park, "Acoustic properties of micro-perforated panel absorbers backed by Helmholtz resonators for the improvement of low-frequency sound absorption," *J. Sound Vib.* **332**, 4895–4911 (2013).
- ⁵⁹O. Abdeljaber, O. Avci, S. Kiranyaz, M. Gabbouj, and D. J. Inman, "Real-time vibration-based structural damage detection using one-dimensional convolutional neural networks," *J. Sound Vib.* **388**, 154–170 (2017).
- ⁶⁰T. Ince, S. Kiranyaz, L. Eren, M. Askar, and M. Gabbouj, "Real-time motor fault detection by 1-d convolutional neural networks," *IEEE Trans. Ind. Electron.* **63**, 7067–7075 (2016).
- ⁶¹S. Kiranyaz, T. Ince, and M. Gabbouj, "Real-time patient-specific ECG classification by 1D convolutional neural networks," *IEEE Trans. Biomed. Eng.* **63**, 664–675 (2015).
- ⁶²H. Lim, J. Park, and Y. Han, "Rare sound event detection using 1d convolutional recurrent neural networks," in *Proceedings of the Detection and Classification of Acoustic Scenes and Events 2017 Workshop* (Tampere University of Technology, Laboratory of Signal Processing, 2017), pp. 80–84.
- ⁶³U. B. Baloglu, M. Talo, O. Yildirim, R. San Tan, and U. R. Acharya, "Classification of myocardial infarction with multi-lead ECG signals and deep CNN," *Pattern Recognit. Lett.* **122**, 23–30 (2019).
- ⁶⁴U. R. Acharya, H. Fujita, S. L. Oh, Y. Hagiwara, J. H. Tan, and M. Adam, "Application of deep convolutional neural network for automated detection of myocardial infarction using ECG signals," *Inform. Sci.* **415**, 190–198 (2017).
- ⁶⁵U. R. Acharya, S. L. Oh, Y. Hagiwara, J. H. Tan, M. Adam, A. Gertych, and R. San Tan, "A deep convolutional neural network model to classify heartbeats," *Comput. Biol. Med.* **89**, 389–396 (2017).
- ⁶⁶A. Arjun, R. Ajith, and S. Kumar Ranjith, "Mixing characterization of binary-coalesced droplets in microchannels using deep neural network," *Biomechanics* **14**, 034111 (2020).
- ⁶⁷B. T. Bastian, N. Jaspreeth, S. K. Ranjith, and C. Jiji, "Visual inspection and characterization of external corrosion in pipelines using deep neural network," *NDT E Int.* **107**, 102134 (2019).
- ⁶⁸A. I. Komkin, M. A. Mironov, and A. I. Bykov, "Sound absorption by a Helmholtz resonator," *Acoust. Phys.* **63**, 385–392 (2017).
- ⁶⁹I. L. Vér and L. L. Beranek, *Noise and Vibration Control Engineering: Principles and Applications* (John Wiley & Sons, 2005).
- ⁷⁰P. Soon-Hong, "A design method of micro-perforated panel absorber at high sound pressure environment in launcher fairings," *J. Sound Vib.* **332**, 521–535 (2013).
- ⁷¹A. Abbad, N. Atalla, M. Ouisse, and O. Doutres, "Numerical and experimental investigations on the acoustic performances of membraned Helmholtz resonators embedded in a porous matrix," *J. Sound Vib.* **459**, 114873 (2019).
- ⁷²J. Allard, *Propagation of Sound in Porous Media: Modelling Sound Absorbing Materials* (Springer, 2012).
- ⁷³J. Ji, D. Li, Y. Li, and Y. Jing, "Low-frequency broadband acoustic metasurface absorbing panels," *arXiv:2002.05325* (2020).